Tunneling rates in electron transport through double-barrier molecular junctions in a scanning tunneling microscope

G. V. Nazin, S. W. Wu, and W. Ho*

Departments of Physics & Astronomy and Chemistry, University of California, Irvine, CA 92697-4575

Edited by Mark A. Ratner, Northwestern University, Evanston, IL, and approved May 16, 2005 (received for review February 10, 2005)

The scanning tunneling microscope enables atomic-scale measurements of electron transport through individual molecules. Copper phthalocyanine and magnesium porphine molecules adsorbed on a thin oxide film grown on the NiAl(110) surface were probed. The single-molecule junctions contained two tunneling barriers, vacuum gap, and oxide film. Differential conductance spectroscopy shows that electron transport occurs via vibronic states of the molecules. The intensity of spectral peaks corresponding to the individual vibronic states depends on the relative electron tunneling rates through the two barriers of the junction, as found by varying the vacuum gap tunneling rate by changing the height of the scanning tunneling microscope tip above the molecule. A simple, sequential tunneling model explains the observed trends.

molecular electronics | vibronic states | single-molecule spectroscopy

Molecule-mediated electron transport is one of the most fundamental phenomenons in nature and is a part of many chemical and biological processes. A considerable amount of research effort has been directed toward the study of electron transport on the single-molecule scale (1–12), where the intrinsic properties of electron transport are particularly apparent. One of these properties is the coupling of tunneling electrons to the nuclear motion (13, 14), with examples including single-molecule chemistry with a scanning tunneling microscope (STM) (14) and vibrational excitation by inelastic electron tunneling (14–16). Recently, tunneling mediated by molecular vibronic levels in field-effect transistors (5–7, 12) and single-molecule junctions defined with STM (17–21) has been observed. These vibronic levels belong to the transient charged state of the molecules, and are thus fundamentally different from the modes seen in the usual inelastic electron tunneling spectroscopy, where vibrations in the final (neutral) molecular state are probed (14, 15, 22). In both field-effect transistor and STM cases, the junction includes two tunneling barriers isolating the molecules from the "source" and "drain" electrodes. These junctions therefore represent model systems for the general case of electron transport through molecules sufficiently isolated electronically from their environment.

Sequential Tunneling Model

Here, we describe experiments on electron transport in STM double-barrier, single-molecule junctions. The junctions were formed by positioning the STM tip over individual molecules adsorbed on an ultrathin [≈5 Å] insulating Al_2O_3 film grown on the NiAl(110) surface (Fig. 1*A*). The two tunnel barriers in the junction are the oxide film and the vacuum gap between the molecule and STM tip. We found that intensities of individual vibronic states observed with differential conductance (dI/dV) spectroscopy were sensitive to the relation between the tunneling rates through the two barriers. Sensitivity of current–voltage (I–V) characteristics to the tunneling rates has been seen for double-barrier transport through metal clusters (23), quantum wells (24), and quantum dots (25, 26), where the presence and/or shape of the Coulomb staircase in I–V depended on the ratio of the two tunneling rates. Analogously to the aforementioned systems, when the coupling to both of the electrodes is small enough, so that the relaxation of the system between the successive tunneling events is faster than the two tunneling rates, the charge transport in molecular double-barrier junctions can be described as sequential hopping of electrons (4, 20, 27).

In the sequential tunneling picture, each event, where one electron passes through the junction, is comprised of two steps (Fig. 1 *B* and *C*). We consider the case of tunneling through the molecular affinity level (the case of the ionization state is analogous), so that the molecule can be either in its neutral state (M^0) or occupied by an electron (M^{-1}). In the first step (Fig. 1*B*), the electron tunnels into the molecule, creating a vibrationally excited M^{-1} state. This step becomes possible when the bias voltage applied to the junction is high enough for the Fermi level of the left electrode to be raised above the affinity level of the molecule. Tunneling into higher-energy vibronic states of M^{-1} occurs at higher biases. Electron injection into the molecule is followed by relaxation to the ground vibrational state of M^{-1}. In the second tunneling step (Fig. 1*C*), the electron leaves the molecule, possibly in a vibrationally excited state, which then decays to the ground vibrational level of M^0 before the injection of the next electron from the left electrode. More complicated scenarios, including incomplete vibrational relaxation between the tunneling events could be considered. Here, we restrict ourselves to the simple but illustrative model of Fig. 1 *B* and *C*, where the system is characterized by two probabilities, P_0 and P_{-1} for the molecule to be in either state M^0 or M^{-1}, correspondingly. In the steady state, probabilities P_{-1} and P_0 do not change with time, and the following formula for the electron current can be written:

$$I = eP_0R_L = eP_{-1}R_R = e\,\frac{R_LR_R}{R_R + R_L},$$

where $e > 0$ is the electron charge, and R_L and R_R are the rates of change in P_0 (and/or P_{-1}) caused by electron transfer from the left electrode into the molecule and from the molecule into the right electrode, respectively. These rates include all possible channels of tunneling corresponding to different vibronic levels of M^0 and M^{-1}:

$$R_L = \Gamma_L \sum_{M^0 \to M^{-1}} f_i \text{ and } R_R = \Gamma_R \sum_{M^{-1} \to M^0} f_i,$$

This paper was submitted directly (Track II) to the PNAS office.

Abbreviations: STM, scanning tunneling microscope; dI/dV, differential conductance; I–V, current–voltage; CuPc, copper phthalocyanine; MgP, magnesium porphine.

*To whom correspondence should be addressed. E-mail: wilsonho@uci.edu.

www.pnas.org/cgi/doi/10.1073/pnas.0501171102

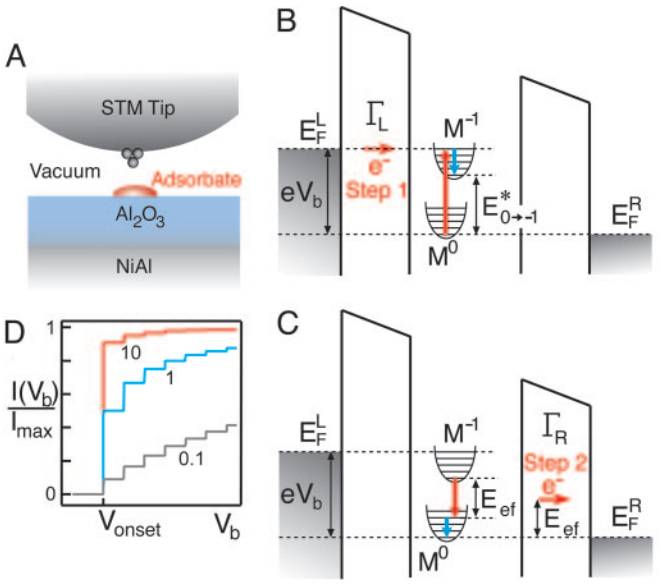

Fig. 1. Electron transport in a double-barrier molecular junction. (*A*) Schematic of a double-barrier, single-molecule STM junction. (*B*) The first step of tunneling through a molecular affinity state M^{-1} in a double-barrier junction. E_F^L and E_F^R show the Fermi levels of the left and right electrodes, respectively. V_b is the voltage applied to the junction, and $e > 0$ is the electron charge. Injection of an electron into the molecule induces a transition from the ground vibrational level of the neutral state M^0 to a vibrationally excited state of M^{-1}, which then decays to the vibrational ground state of M^{-1}. The energy of transition between the ground vibrational levels of M^0 and M^{-1} is given by $E^*_{0\to-1}$, a value affected by the voltage drop in the right barrier (see Fig. 3). (*C*) The electron leaves the molecule in a vibrationally excited state of M^0 (second tunneling step), which decays to the ground vibrational level of M^0. E_{ef} is the final energy of the electron. (*D*) *I–V* curves ($V_b > 0$) of a model double-barrier molecular junction for different ratios Γ_L/Γ_R, as shown next to the corresponding curves. The curves were normalized by using their asymptotic high V_b values. The onset of conduction is at V_{onset}.

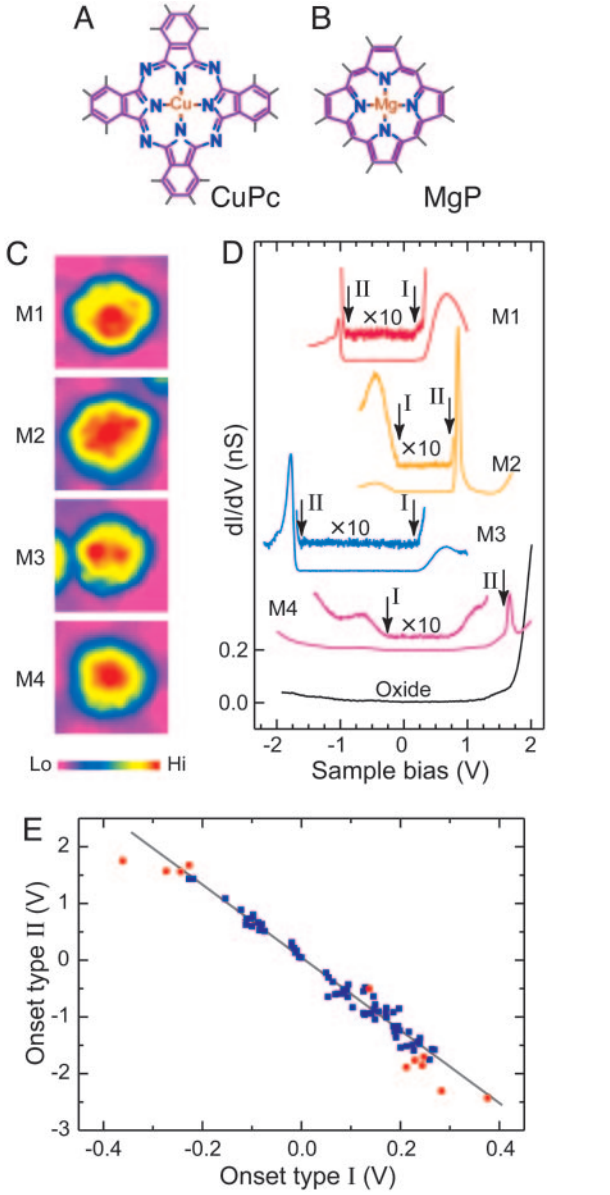

Fig. 2. Adsorption configurations of CuPc and MgP and bipolar tunneling. (*A* and *B*) Molecular structures of CuPc and MgP, respectively. (*C*) STM topographic images of two different conformations of CuPc (M1 and M2, $V_b = 2.0$ V and $I = 0.1$ nA) and MgP (M3 and M4, $V_b = 2.25$ V and $I = 0.1$ nA) adsorbed on the oxide surface. The scan size is 39 Å by 39 Å. (*D*) dI/dV spectra measured with the STM tip positioned over the centers of the four molecules in *C*. A spectrum measured on the clean oxide surface is shown for comparison. The conductance onsets at opposite bias polarities are marked by I (broad band onset) and II (sharp peak onset). The spectra for all molecules are offset for clarity. The tunneling gap for every molecule was set to be the same as in *C*. (*E*) Plot showing the correlation of type I and II spectral features. Onset type I and onset type II for 73 different CuPc (■), and 11 MgP (●) molecules. Many of the molecules correspond to other types of adsorption configurations, not shown in *C*. Even though the STM image and dI/dV spectra of M2 appear similar to those reported in ref. 17, M2 represents a different type of adsorption.

where f_i is the corresponding Franck-Condon factors of the vibronic states (28) and Γ_L and Γ_R are the tunneling rates responsible for electronic coupling between the molecule and two electrodes in the junction (27). The summations run over the vibronic states available for tunneling. Here, for the purpose of our qualitative consideration, we assumed the temperature in the junction to be much less than the characteristic vibrational energies. We also ignored the spectral structure of each vibronic state and neglected the dependence of Γ_L and Γ_R on the applied bias V_b (see Fig. 1 *B* and *C*).

Rates R_L and R_R are bias-dependent and increase stepwise (the height of each step is proportional to the corresponding f_i factor) with increasing V_b every time a new vibronic channel becomes available for tunneling. The heights of the corresponding steps in the tunneling current are modulated by the R_L/R_R ratio. This modulation is illustrated in Fig. 1*D*, where tunneling current for different ratios of Γ_L and Γ_R is shown for a fictitious system, where $R_R = \Gamma_R$ is constant,[†] and f_i factors in R_L are equidistant in V_b and have equal values. When $\Gamma_L \ll \Gamma_R$ (bottom curve in Fig. 1*D*) we have that $I(V) \approx eR_L(V)$, so that the steps in the *I–V* curve reflect the f_i factors of individual vibronic levels in R_L. On the other hand, for $\Gamma_L \gg \Gamma_R$ (top curve in Fig. 1*D*) the current is limited by the right barrier, and $I(V)$ rises to its maximum value, $e\Gamma_R$, already at the onset of conduction, so that any further increase in R_L associated with opening of new vibronic channels does not affect the current. Both limits are observed in the STM junctions (20), as discussed below.

Bipolar Tunneling

The experiments were carried out with a home-built ultrahigh-vacuum STM operated at 15 K (29). The NiAl(110) surface was

[†] R_R can be nearly constant when the molecular level is high enough above the Fermi level of the unbiased junction, so that all vibrational channels with appreciable Frank-Condon factors are open in R_R.

prepared by cycles of Ne^+ sputtering and annealing to 1,300 K, and then oxidized to obtain a thin Al_2O_3 film covering ≈50% of the NiAl(110) surface. The molecules were thermally evaporated on the oxidized surface at 15 K. Copper phthalocyanine (CuPc, Fig. 2*A*) and magnesium porphine (MgP, Fig. 2*B*) molecules were studied. The Al_2O_3 film has a large unit cell (18 Å by 11 Å) (30), giving rise to different types of molecular adsorption configurations. Depending on the nature of adsorption, specific STM images (Fig. 2*C*) and dI/dV spectra are expected (Fig. 2*D*). (For all STM images and dI/dV spectra positive bias voltage V_b corresponds to electrons tunneling from the tip into the sample.) The differential conductance spectra were obtained by using the lock-in technique, with 10-mV (rms) modulation of the sample bias at 400 Hz. The bias voltages in these spectra were limited to avoid perturbation of the molecules. Higher bias voltages (or sufficiently high tunneling currents) resulted in switching from one adsorption configuration to another and/or molecular motion on the surface, similar to the situation described in refs. 17 and 31. Desorption of CuPc and MgP, except at very close tip-sample separations, was found to be relatively unlikely. This stability appears to be caused by the electrostatics of CuPc and MgP (which are charge transfer complexes) on the oxide surface, since nonpolar species (for example, noble metal atoms and small clusters, aromatic hydrocarbon molecules) could be easily desorbed from the surface as was found in separate experiments.

The dI/dV spectra measured on all molecules typically show two types of spectral features. Type I is represented by relatively broad bands, as seen for M1 and M3 when $V_b > 0$, as well as for M2 and M4 when $V_b < 0$. For CuPc, these bands have been previously attributed to tunneling through the vibronic levels (17, 20), analogously to Fig. 1*B*. Type II includes sharp peaks seen for M1 and M3 when $V_b < 0$, as well as for M2 and M4 when $V_b > 0$. For every molecule, type I and II dI/dV features appear together at opposite bias polarities, with the magnitudes of the bias voltages corresponding to the onset of type II features always being five to 10 times higher than that of the type I features. In the bandgap between the two types of bands, the conduction is close to zero (except M4 in Fig. 2, which has an additional type I band for $V_b > 0$). We plotted the voltages of these onsets against each other for 73 different CuPc and 11 different MgP molecules (Fig. 2*E*).

The data of Fig. 2*E* fall on one line, suggesting that both type I and II bands in a particular dI/dV curve are produced by tunneling through the same molecular states. Indeed, let us consider the case of conduction through M^{-1} (Figs. 1 *B* and *C* and 3 *A* and *B*). Because M^{-1} is tied to the vacuum level in the junction, tunneling through M^{-1} is also possible when the polarity of V_b is reversed and electron injection into the molecule occurs through the right barrier. The voltages corresponding to onsets of conduction at the two polarities will be determined by the amounts of the voltage drops in the two barriers. Denoting αV_b as the voltage drop in the right barrier ($\alpha < 1$), we obtain that electron injection from the left electrode will occur when

$$|V_b| = \frac{E_{0\to-1}}{e(1-\alpha)},$$

where $E_{0\to-1}$ is the energy of the affinity level with respect to the Fermi level of the unbiased junction. Electron injection from the right electrode occurs at the opposite polarity at

$$|V_b| = \frac{E_{0\to-1}}{e\,\alpha}.$$

Thus, conduction through the same state is possible at either bias polarity (5–12, 20, 32, 33), with the ratio of the two onset voltages being $(1-\alpha)/\alpha$. In a similar fashion, we arrive at the same conclusion regarding conduction through the ionization states M^{+1} (Fig. 3 *C* and *D*). In the present case, the correlation seen in Fig. 2*E* is therefore caused by the single-molecule junctions having similar α, but different $E_{0\to-1}$ (for the data points corresponding to conduction through the affinity states) and $E_{0\to+1}$ (for the data points corresponding to the ionization states). Factor α_{oxide} ($\alpha_{oxide}V_b$ gives the voltage drop on the oxide side of the junction) is expected to be small because of the large effective dielectric constant of the oxide film (≈10 for bulk alumina) and the fact that the oxide thickness is comparable to the tip-molecule separation. The observed ratio of onsets for type I and II features varies from 5 to 10, which suggests that type I features must involve electron transfer between the tip and molecule as the initial tunneling step, whereas for type II features the initial tunneling step is electron transfer between NiAl and molecule (Fig. 3). Thus, M1 and M3 correspond to tunneling through the affinity states (Fig. 3 *A* and *B*), whereas in M2 and M4 tunneling through the ionization states is observed (Fig. 3 *C* and *D*). [Here, we speak of the affinity and ionization states of adsorbed molecules, which can be affected by the possible permanent charging of the molecules (34).]

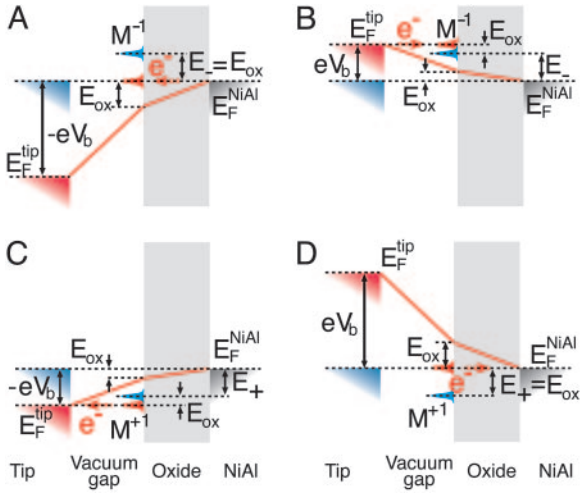

Fig. 3. Diagrams showing conduction through the affinity (M^{-1}) and ionization (M^{+1}) molecular states for $V_b < 0$ (*A* and *C*) and $V_b > 0$ (*B* and *D*). The ground vibrational states of M^{+1} and M^{-1} (which in the unbiased junction have energies E_+ and E_-, respectively) as well as the NiAl and tip Fermi levels E_F^{NiAl} and E_F^{tip} are shown for the unbiased ($E_F^{NiAl} = E_F^{tip}$) and biased ($E_F^{NiAl} \neq E_F^{tip}$) junctions, with E_F^{NiAl} level taken as a reference. The electrostatic potential profiles in the biased junction are shown by the solid sloped lines. All diagrams correspond to the first step of tunneling. *A* and *B* represent the case of M1 and M3, and *C* and *D* show the conduction through M2 and M4. E_{ox} is given by $E_{ox} = \alpha_{oxide}\, eV_b$ and represents the shift of the M^{+1} and M^{-1} levels with respect to E_F^{NiAl} caused by the voltage drop across the oxide.

dI/dV Spectra for Different Tip-Molecule Tunneling Rates

Even though type I and II bands correspond to tunneling through the same states, their spectral shapes are dramatically different. Because every type of tunneling is associated with charge injection through a particular barrier at the first step (Fig. 3), it is feasible that the properties of the two tunneling barriers themselves might be responsible for the differences between type I and II bands. To investigate this possibility we vary the tunneling barrier corresponding to the tip-molecule gap by changing the tip-sample separation Z. The corresponding data for CuPc molecules are shown in Figs. 4 (for molecule M1) and 5 (for molecule M2). The case of MgP is shown in Figs. 6 (for molecule M3) and 7 (for molecule M4). In all figures, the smallest attainable Z was limited by the molecular instability.

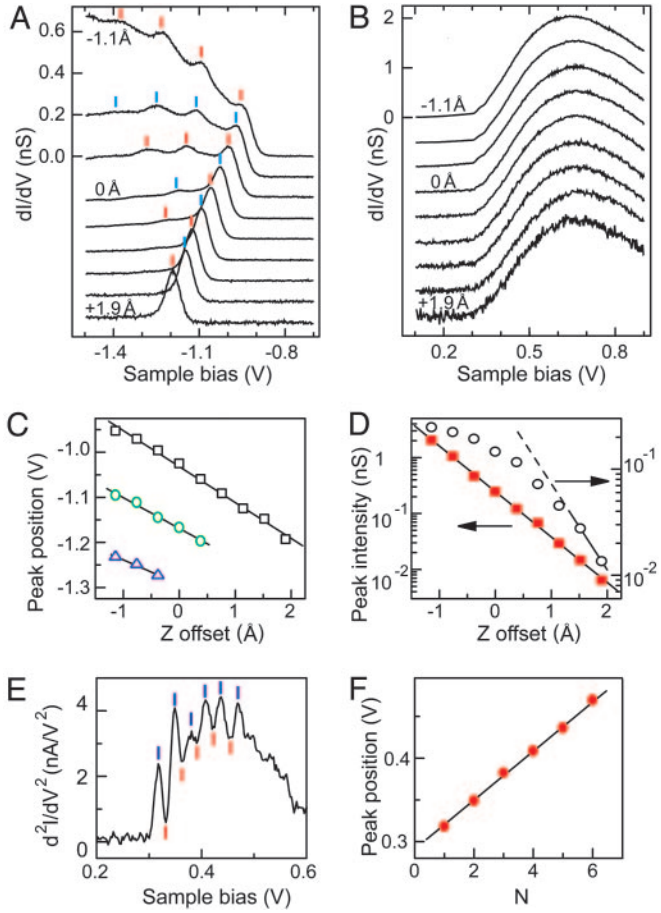

Fig. 4. Conduction through molecule M1 (Fig. 2). (*A* and *B*) dI/dV spectra for different tip-molecule separations Z for $V_b < 0$ and $V_b > 0$, respectively. Z-offsets, referenced to the gap set with $V_b = 2.0$ V, $I = 0.1$ nA, were applied incrementally ranging from −1.1 to +1.9 Å. The spectra (except the topmost spectra) were scaled by different factors and offset for clarity. Peaks corresponding to the vibronic states of M1 are marked by the vertical dashes. (*C*) Positions of the first three peaks observed in *A* as a function of Z-offset. (*D*) dI/dV peak intensities from *A* and *B* as a function of Z-offset. ■ correspond to the band intensity maximum in *B*, and ○ correspond to the intensity of the first peak in *A*. (*E*) d^2I/dV^2 spectrum measured concurrently with the second spectrum from the top in *B*. (*F*) Positions of the peaks from *E* as a function of the number of the peak. The peak spacing is 29 ± 2 mV.

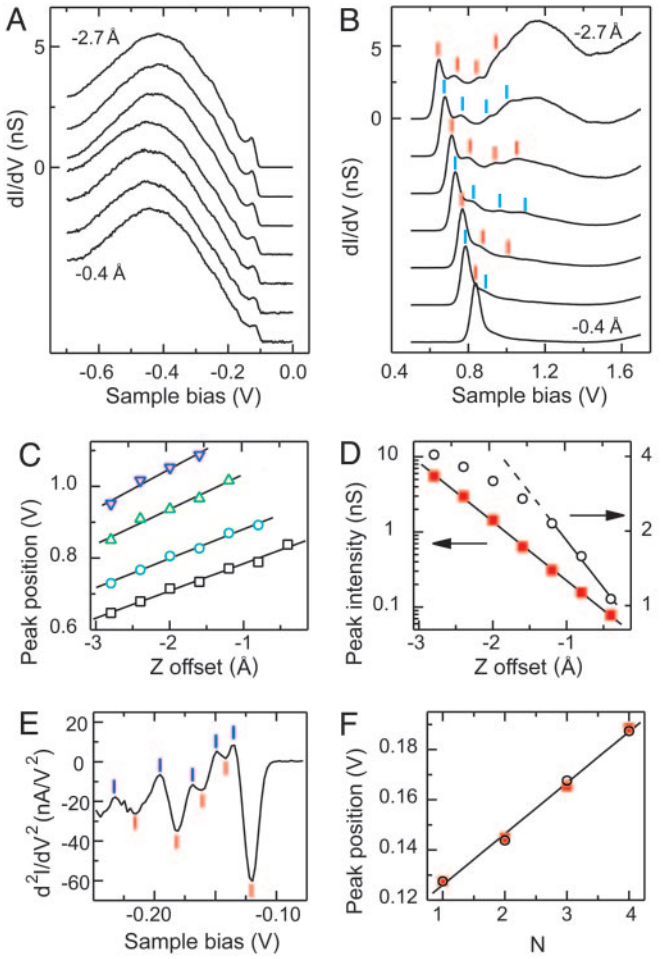

Fig. 5. Conduction through molecule M2 (Fig. 2), measured and presented analogously to Fig. 4. (*A* and *B*) dI/dV spectra for different tip-molecule separations Z. Z-offsets range from −2.7 to −0.4 Å. (*C*) Positions of the four peaks observed in *B* as a function of Z-offset. (*D*) dI/dV peak intensities from *A* and *B* as a function of Z-offset. ■ correspond to the band intensity maximum in *A*, and ○ correspond to the intensity of the first peak in *B*. (*E*) d^2I/dV^2 spectrum measured concurrently with the top spectrum in *A*. (*F*) Absolute values of positions of the type I peaks determined from *E* (■) together with the peaks from the top curve of *B* scaled down by 5.07 (○), presented as functions of the number of the peak. The spacing for peaks from *E* is 20.3 ± 0.9 mV.

As seen in Figs. 4–7, every type II band consists of only a single sharp peak when Z is large (bottom curves in Figs. 4*A*, 5*B*, 6*A*, and 7*A*). For smaller separations, additional equally spaced peaks appear in the dI/dV (top curves in Figs. 4*A*, 5*B*, 6*A*, and 7*A*), and the bands shift toward $V_b = 0$. We note that the direction of the shift is consistent with the model of tunneling shown in Fig. 3*A* (for M1 and M3) and Fig. 3*D* (for M2 and M4). For this type of tunneling, the shift is caused by the Z-dependence of $1/\alpha_{oxide}$, which increases with Z. The shift is linear for all molecules (Figs. 4*C*, 5*C*, 6*B*, and 7*B*), which could be expected when the curvature of the tip as well as the lateral molecular dimensions are large as compared with the tip-sample distance (parallel plate capacitor model).

The overall shape and position of type I spectral features for all molecules in Fig. 2 did not change noticeably with Z, as shown in Figs. 4*B* and 5*A* for CuPc. The absence of shift is consistent with the presented electrostatic model. The shift of type I bands is expected to be $(1 - \alpha)^2/\alpha^2$ times smaller than that of type II. For different molecules this formula gives numbers in the range of 25 to 100, so that the shift of the type I band is on the order of 1–2 meV. Type I bands contain weak structures, attributable to vibronic levels of the transiently charged states of the molecules. This weak structure is revealed by recording second derivatives of I–V curves, as presented in Figs. 4 *E* and *F* and 5 *E* and *F*, where equidistant peaks and dips reminiscent of vibrational progressions are seen. Because vibronic states should appear as peaks in dI/dV, every peak-dip pair should correspond to a vibronic state. This state should be located midway between the peak and dip. Tunneling through these vibronic states generally occurs at bias voltages proportional to those corresponding to peaks in the type II bands. Thus, for M1 the ratio of spacings for type I and type II peaks is 4.8 ± 0.3, consistent with that of the onsets (6.5 ± 1.8). For M2, positions of type II peaks are proportional to voltages found for type I peaks within a factor of 5.07 ± 0.4 (Fig. 5*F*). Therefore, peaks in type II bands should correspond to conduction through the same vibronic states as those of type I bands. Taking into account voltage division in the junction, the peak spacing found in Fig. 4*F* (29 ± 2 mV) gives a value of 24 ± 2.2 meV for the vibrational energy, which is in the range of CuPc macrocycle bending and in-phase

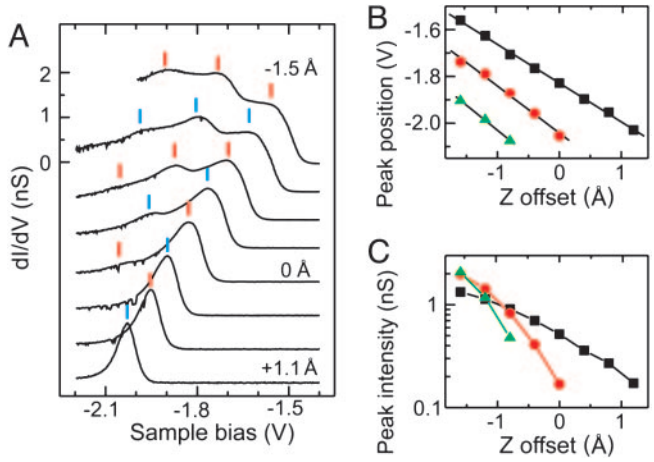

Fig. 6. Conduction through molecule M3 (Fig. 2). (*A*) dI/dV spectra for different tip-molecule separations Z for $V_b < 0$. Z-offsets, referenced to the gap set with $V_b = 2.25$ V, $I = 0.1$ nA, were applied incrementally ranging from -1.5 to $+1.1$ Å. The spectra (except the topmost spectrum) were scaled by different factors and offset for clarity. Peaks corresponding to the vibronic states of M3 are marked by vertical dashes. The shape of the band seen at $V_b > 0$ in Fig. 2*D* does not change with Z-offset. (*B*) Positions of the three peaks observed in *A* as a function of Z-offset. (*C*) Peak intensities from *A* as a function of Z-offset. The different peaks are shown with the same symbols as in *B*.

movement of pyrrole groups (35). The spacing of the peaks observed in Fig. 5*E* (20.3 ± 0.9 mV) gives 17 ± 1.5 meV, which is close to the vibrational energy of isoindole bending in CuPc (36). Type I bands of MgP molecules did not show any clear vibrational structure (checked with bias modulation amplitude of 5 mV rms), even though distinct peaks are seen in their type II bands. The peak spacings in the spectra of Figs. 6*A* and 7*A* are 172 ± 3 and 66 ± 3 mV, respectively. With conduction onset ratios of 7.26 ± 0.54 and 5.87 ± 0.13, vibrational energies of 23.7 ± 2.4 and 11.2 ± 1.2 meV are obtained for M3 and M4, respectively, consistent with vibrations associated with pyrole deformation and dome-type deformation of porphines (36).

The observed vibrational peaks have relatively large widths and are normally seen on top of a broad background. It is likely

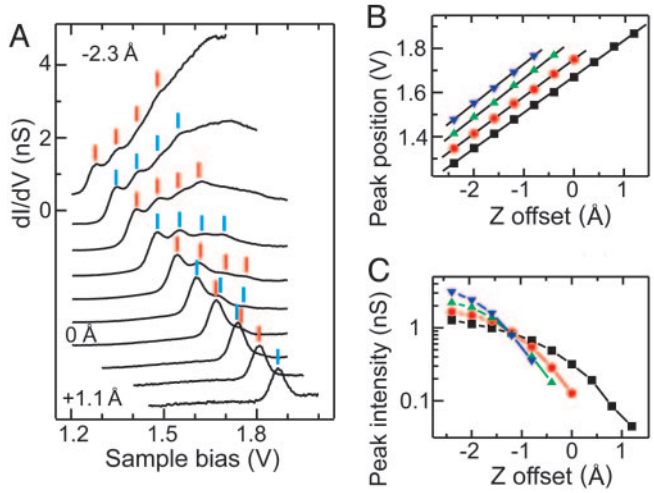

Fig. 7. Conduction through molecule M4 (Fig. 2). (*A*) dI/dV spectra measured and presented analogously to Fig. 6 ($V_b > 0$). Z-offsets range from -2.3 to $+1.1$ Å. The shape of the band seen at $V_b < 0$ in Fig. 2*D* does not change with Z-offset. (*B*) Positions of the four peaks observed in *A* as a function of Z-offset. (*C*) Peak intensities from *A* as a function of Z-offset.

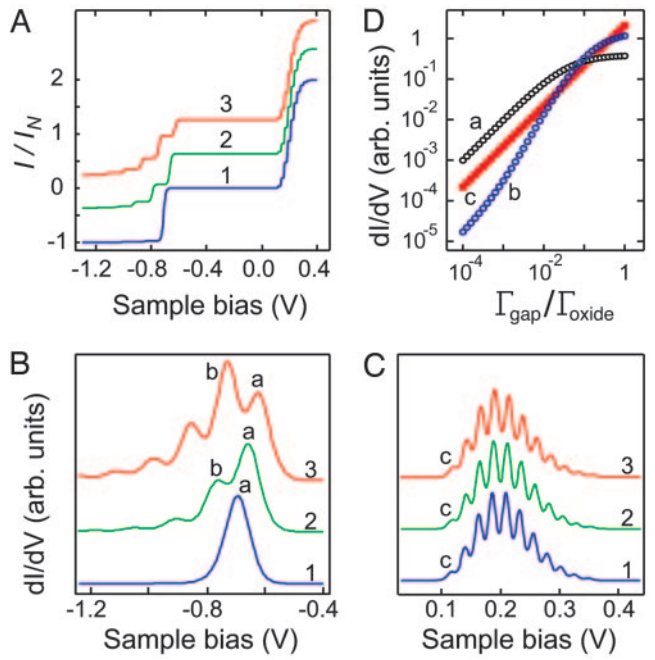

Fig. 8. Numerically simulated conduction through the affinity state of a molecule in a double-barrier junction. The calculations were performed by using the model from ref. 27 with coupling to a single vibrational mode with energy $\hbar\omega = 20$ meV, but without damping, M^{-1} state is assumed to be doubly spin degenerate. (*A*) *I–V* curves for three different tip-molecule separations Z, corresponding to $\alpha_{oxide} = 0.14$, 0.15, and 0.16 for curves 1, 2, and 3, respectively. The ratios of the tunneling rates for the vacuum gap and oxide were taken to be $\Gamma_{gap}/\Gamma_{oxide} = 0.001$, 0.03, and 0.1, respectively; $k_BT = 0.05\ \hbar\omega$, $E_- = 5\ \hbar\omega$ (see Fig. 3 *A* and *B*), $g = 4$ (Frank-Condon displacement parameter). The current for each curve was normalized by $I_N = e\Gamma_{gap}\Gamma_{oxide}/(\Gamma_{gap} + \Gamma_{oxide})$. (*B* and *C*) dI/dV spectra corresponding to the *I–V* curves in *A*. Analogously to Fig. 4, curves in were scaled. Higher temperature parameter ($k_BT = 0.2\ \hbar\omega$) was used for these curves. Curves numbered 2 and 3 in *A–C* were offset for clarity. (*D*) Logarithmic plot of intensities of peaks a, b, and c from *B* and *C*, as a function of $\Gamma_{gap}/\Gamma_{oxide}$ ratio.

that the dI/dV spectra are envelopes of many vibronic states, probably coupled to other molecular vibrations and the environment (for example, the phonon modes of the oxide film). Measurements on many molecules showed that the vibrational mode that is the most visible in the spectrum of a molecule is apparently determined by the type of adsorption configuration of the molecule (molecules that appear similar in STM images typically show similar dI/dV spectra).

Numerical Simulations

The variation in the intensity of the type II sideband with Z in Figs. 4–7 can be understood by using the tunneling rate model of Fig. 1, assuming that for large Z tunneling through the oxide layer is much faster than through the vacuum gap. Fig. 1 *B* and *C* correspond to conduction through the affinity state (molecules M1 and M3). The case of the ionization state (molecules M2 and M4) is considered analogously. Numerical simulations of *I–V* and dI/dV characteristics obtained by using this model are presented in Fig. 8.

When $V_b > 0$, in the first tunneling step an electron is injected into the molecule through the vacuum gap (Fig. 3*B*). The vacuum gap then serves as the left barrier in Fig. 1 *B* and *C*, whereas the oxide is the right barrier, so that $\Gamma_L \ll \Gamma_R$. This limit is the case of the bottom curve in Fig. 1*D*, where the intensities of individual conduction channels in the resulting *I–V* curve are only weakly affected by the presence of the right barrier. The *I–V* corresponding to the present case is the bottom curve ($V_b > 0$) in Fig.

8*A*, which shows a sequence of steps caused by tunneling into individual vibronic channels of M^{-1}. The corresponding dI/dV spectrum in Fig. 8*C* (bottom curve) shows these vibronic states as peaks (only one vibrational mode is considered in the simulation, so that the simulated dI/dV peaks appear relatively sharp).

When $V_b < 0$, and in the first tunneling step an electron is injected through the oxide (Fig. 3*A*), oxide becomes the left barrier in Fig. 1 *B* and *C*, whereas the vacuum gap becomes the right barrier, so that $\Gamma_L \gg \Gamma_R$. Then, as for the top curve in Fig. 1*D*, the *I–V* should be dominated by a single step, which is exactly what is observed in the bottom curve of Fig. 8*A* for $V_b < 0$. Therefore, the dI/dV is dominated by a single peak (bottom curve in Fig. 8*B*), with all other higher-energy vibronic peaks being suppressed. This suppression is similar to the case of large *Z* (when the tunneling rate through the vacuum gap is small) in Figs. 4*A* and 6*A*. When *Z* is decreased, the tunneling rate through the vacuum gap increases and can become comparable to that through the oxide, so that the situation corresponding to the middle curve in Fig. 1*D* can be realized for both bias polarities. Higher-energy vibronic states would then be more visible for $V_b < 0$. In accordance with this idea, Fig. 8*B* shows a gradual emergence of vibronic sidebands with smaller *Z* (and emergence of steps in *I–V* in Fig. 8*A*), reproducing the trends seen in Figs. 4*A* and 6*A*. On the other hand, the spectral shapes of type I bands in Figs. 4*B* and 5*A* are not visibly affected by *Z*-variation, which suggests that even at the smallest *Z*, tunneling through the oxide is still considerably faster than through the vacuum gap. Fig. 8*C* shows that in these conditions the spectral shape of the type I bands is not affected by variations in the tunneling rate through the vacuum gap.

Additional support to the presented sequential tunneling model is provided by the variation of the intensities of type I and II peaks with *Z*. Type I peaks show exponential increase in intensity when *Z* is decreased (Figs. 4*D* and 5*D*), whereas type II peaks deviate from exponential for smaller *Z* (Figs. 4*D*, 5*D*, 6*C*, and 7*C*). Similar trends are seen in Fig. 8*D*. The differences in *Z*-dependence for type I and II peaks are attributed to the fact that for the two opposite bias polarities the total number of vibronic states available for tunneling through a particular barrier is different. For example, for type II peak, during tunneling through the oxide (first step), only M^{-1} vibronic states at the very onset of conduction are available, whereas for type I band, in tunneling through the oxide (second step) many vibrational states of M^0 are available. In a similar fashion, the apparent differences between the different type II peaks belonging to the same band (higher energy peaks begin to deviate from exponential at slightly smaller *Z*, see Figs. 6*C*, 7*C*, and 8*D*) are attributed to the larger number of vibronic channels available at the first step of tunneling.

Other *Z*-sensitive factors that could affect the intensity of individual vibronic states in dI/dV spectra are the nonequilibrium population of vibronic states excited by electron tunneling, which is sensitive to the current (19), and the possible dependence of the Frank-Condon factors on the electric field in the junction. Simple considerations shows that neither of the two factors can explain the observed asymmetry between the type I and II bands together with the *Z*-dependence of type II features. These factors, however, may need to be included in a quantitative treatment of conduction in the present double-barrier system. Other factors that need to be considered are the intramolecular vibrational redistribution, vibrational energy dissipation (27), and relaxation of the oxide ionic lattice upon charging of the molecules (34). The merit of our qualitative model is the ability to explain at the simplest possible level the variation in the intensity of vibronic dI/dV peaks as a consequence of the dependence on the tunneling rates.

The suppression of the vibronic peaks in conduction through asymmetric STM junctions has been demonstrated for tunneling both through affinity and ionization states of CuPc and MgP. Similar behavior has been observed in other double-barrier systems studied by our group, for example, Ag-doped C_{60} monolayers on the partially oxidized NiAl surface (21). The diversity of systems exhibiting this effect points to its general nature.

This material is based on work supported by Chemical Science, Geoscience, and Bioscience Division, Office of Science, U.S. Department of Energy Grant DEFG03-01ER15157 and National Science Foundation Grant 0102887.

1. Cui, X. D., Primak, A., Zarate, X., Tomfohr, J., Sankey, O. F., Moore, A. L., Moore, T. A., Gust, D., Harris, G. & Lindsay, S. M. (2001) *Science* **294,** 571–574.
2. Reichert, J., Ochs, R., Beckmann, D., Weber, H. B., Mayor, M. & von Lohneysen, H. (2002) *Phys. Rev. Lett.* **88**, 176804.
3. Xu, B. & Tao, N. J. (2003) *Science* **301,** 1221–1223.
4. Porath, D., Levi, Y., Tarabiah, M. & Millo, O. (1997) *Phys. Rev. B* **56,** 9829–9833.
5. Park, H., Park, J., Lim, A. K. L., Anderson, E. H., Alivisatos, A. P. & McEuen, P. L. (2000) *Nature* **407,** 57–60.
6. Zhitenev, N. B., Meng, H. & Bao, Z. (2002) *Phys. Rev. Lett.* **88**, 226801.
7. Park, J., Pasupathy, A. N., Goldsmith, J. I., Chang, C., Yaish, Y., Petta, J. R., Rinkoski, M., Sethna, J. P., Abruna, H. D., McEuen, P. L. & Ralph, D. C. (2002) *Nature* **417,** 722–725.
8. Liang, W.J., Shores, M.P., Bockrath, M., Long, J. R. & Park, H. (2002) *Nature* **417,** 725–729.
9. Kubatkin, S., Danilov, A., Hjort, M., Cornil, J., Bredas, J. L., Stuhr-Hansen, N., Hedegard, P. & Bjornholm, T. (2003) *Nature* **425,** 698–701.
10. Nitzan, A. & Ratner, M. A. (2003) *Science* **300,** 1384–1389.
11. Yu, L. H., Keane, Z. K., Ciszek, J. W., Cheng, L., Stewart, M. P., Tour, J. M. & Natelson, D. (2004) *Phys. Rev. Lett.* **93,** 266802.
12. Pasupathy, A. N., Park, J., Chang, C., Soldatov, A. V., Lebedkin, S., Bialczak, R. C., Grose, J. E., Donev, L. A. K., Sethna, J. P., Ralph, D. C. & McEuen, P. L. (2005) *Nano Lett.* **5,** 203–207.
13. Seideman, T. (2003) *J. Phys. Condens. Matter* **15,** R521–R549.
14. Ho, W. (2002) *J. Chem. Phys.* **117,** 11033–11061.
15. Hansma, P. K. (1977) *Phys. Rep.* **30,** 145–206.
16. Stipe, B. C., Rezaei, M. A. & Ho, W. (1998) *Science* **280,** 1732–1735.
17. Qiu, X. H., Nazin, G. V. & Ho, W. (2004) *Phys. Rev. Lett.* **92,** 206102.
18. Liu, N., Pradhan, N. A. & Ho, W. (2004) *J. Chem. Phys.* **120,** 11371–11375.
19. LeRoy, B. J., Lemay, S. G., Kong, J. & Dekker, C. (2004) *Nature* **432,** 371–374.
20. Wu, S. W., Nazin, G. V., Chen, X., Qiu, X. H. & Ho, W. (2004) *Phys. Rev. Lett.* **93,** 236802.
21. Nazin, G. V., Qiu, X. H. & Ho, W. (2005) *J. Chem. Phys.*, in press.
22. Galperin, M., Ratner, M. A. & Nitzan, A. (2004) *J. Chem. Phys.* **121,** 11965–11979.
23. Hanna, A. E. & Tinkham, M. (1991) *Phys. Rev. B* **44,** 5919–5922.
24. Su, B., Goldman, V. J. & Cunningham, J. E. (1992) *Science* **255,** 313–315.
25. Katz, D., Millo, O., Kan, S. H. & Banin, U. (2001) *Appl. Phys. Lett.* **79,** 117–119.
26. Bakkers, E. P. A. M., Hens, Z., Zunger, A., Franceschetti, A., Kouwenhoven, L. P., Gurevich, L. & Vanmaekelbergh, D. (2001) *Nano Lett.* **1,** 551–556.
27. Braig, S. & Flensberg, K. (2003) *Phys. Rev. B* **68,** 205324.
28. Schatz, G. C. & Ratner, M. A. (1993) *Quantum Mechanics in Chemistry* (Prentice–Hall, Englewood Cliffs, NJ).
29. Stipe, B. C., Rezaei, M. A. & Ho, W. (1999) *Rev. Sci. Instrum.* **70,** 137–143.
30. Stierle, A., Renner, F., Streitel, R., Dosch, H., Drube, W. & Cowie, B. C. (2004) *Science* **303,** 1652–1656.
31. Qiu, X. H., Nazin, G. V. & Ho, W. (2003) *Science* **299,** 542–546.
32. Datta, S., Tian, W. D., Hong, S. H., Reifenberger, R., Henderson, J. I. & Kubiak, C. P. (1997) *Phys. Rev. Lett.* **79,** 2530–2533.
33. Niquet, Y. M., Delerue, C., Allan, G. & Lannoo, M. (2002) *Phys. Rev. B* **65,** 165334.
34. Repp, J., Meyer, G., Olsson, F. E. & Persson, M. (2004) *Science* **305,** 493–495.
35. Palys, B. J., Vandenham, D. M. W., Briels, W. & Feil, D. (1995) *J. Raman Spectrosc.* **26,** 63–76.
36. Tsai, H. H & Simpson, M. C. (2003) *J. Phys. Chem. A* **107,** 526–541.